

Dalton Transactions

Accepted Manuscript



This is an *Accepted Manuscript*, which has been through the Royal Society of Chemistry peer review process and has been accepted for publication.

Accepted Manuscripts are published online shortly after acceptance, before technical editing, formatting and proof reading. Using this free service, authors can make their results available to the community, in citable form, before we publish the edited article. We will replace this *Accepted Manuscript* with the edited and formatted *Advance Article* as soon as it is available.

You can find more information about *Accepted Manuscripts* in the [Information for Authors](#).

Please note that technical editing may introduce minor changes to the text and/or graphics, which may alter content. The journal's standard [Terms & Conditions](#) and the [Ethical guidelines](#) still apply. In no event shall the Royal Society of Chemistry be held responsible for any errors or omissions in this *Accepted Manuscript* or any consequences arising from the use of any information it contains.

Figure

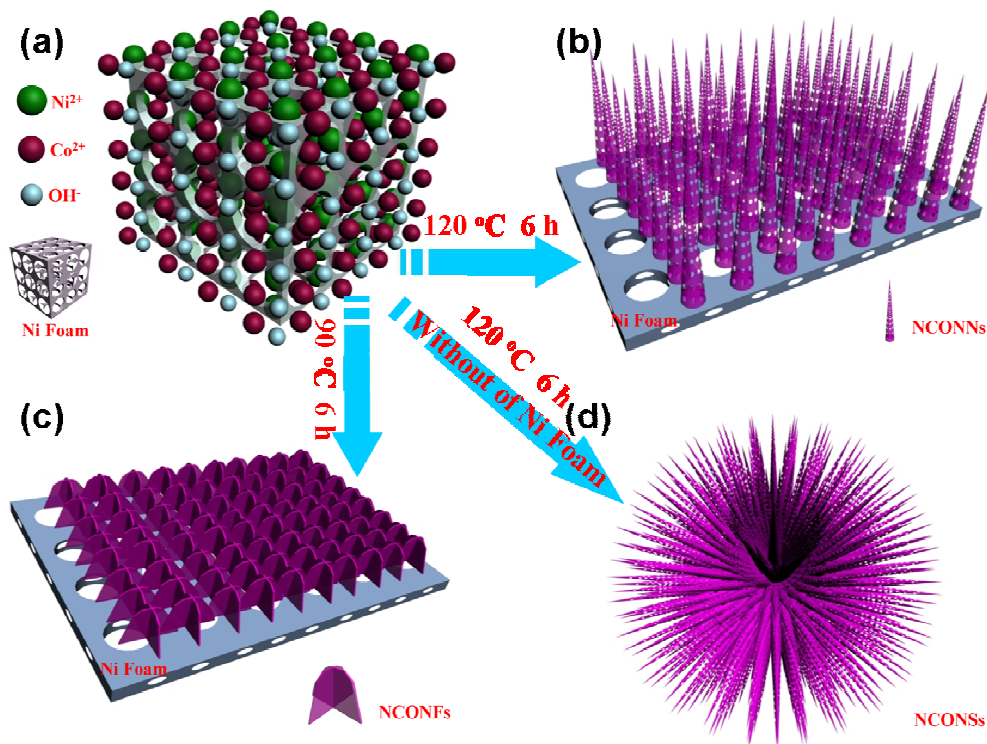


Fig. 1 Schematic illustrating the fabrication processes of the NiCo₂O₄ with three different morphologies. (a) The functionalization process of NiCo₂O₄ anode materials in solution; (b) NCONNs; (c) NCONFs; (d) NCONSs.

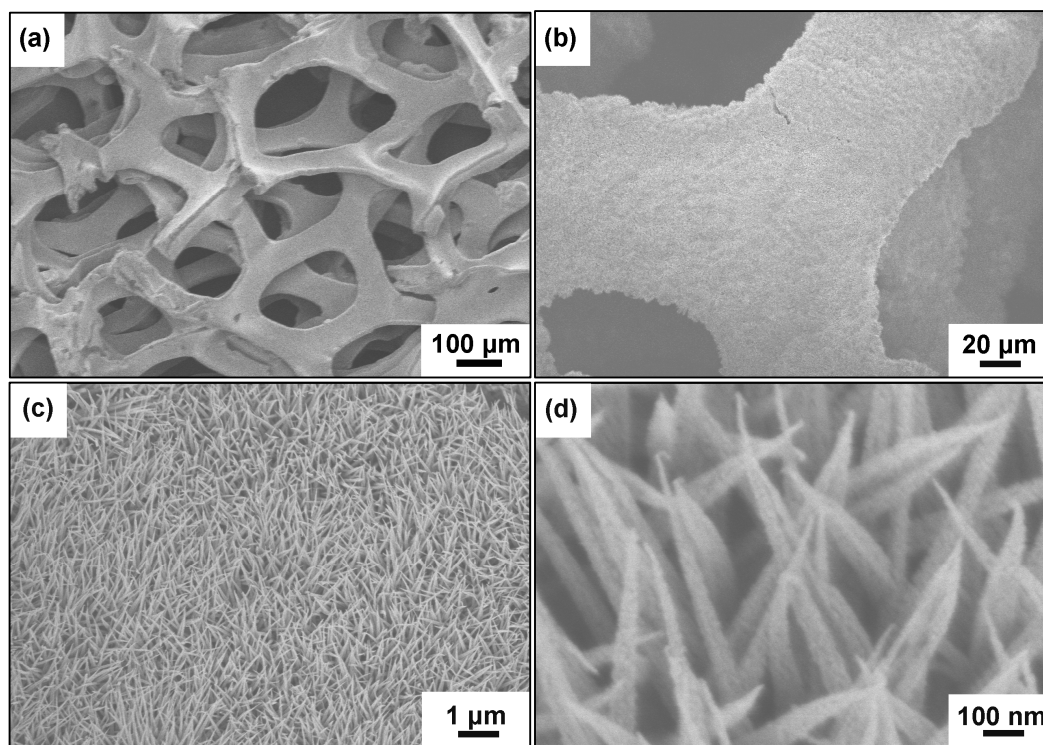


Fig. 2 Representative FESEM images of the NCONNs grown on Ni foam. (a) SEM image of the well-cleaned Ni Foam; (b) SEM image of Ni Foam after coating of NCONNs; (c,d) High-magnification SEM image of NCONNs.

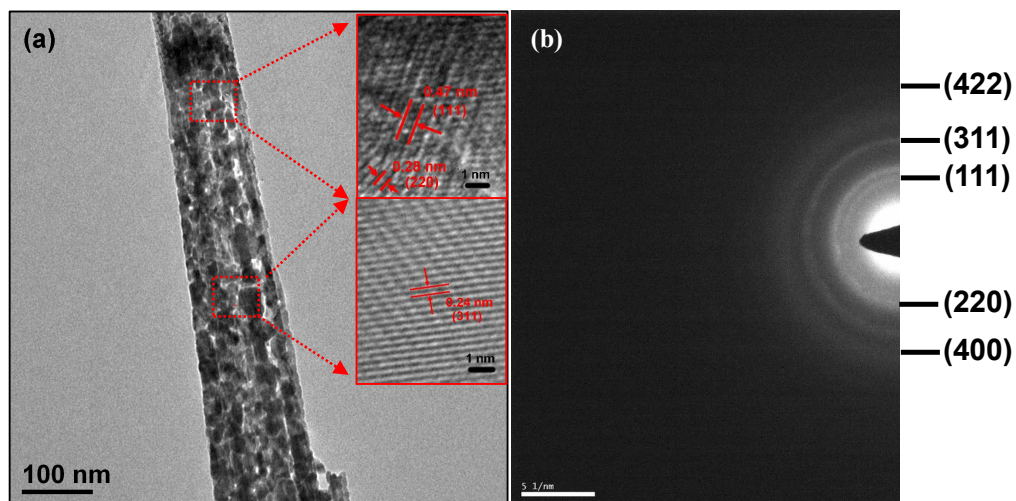


Fig. 3 (a) Low-magnification and high-magnification (insets) TEM images of the NCONNs; (b) the corresponding SAED patterns from NiCo₂O₄.

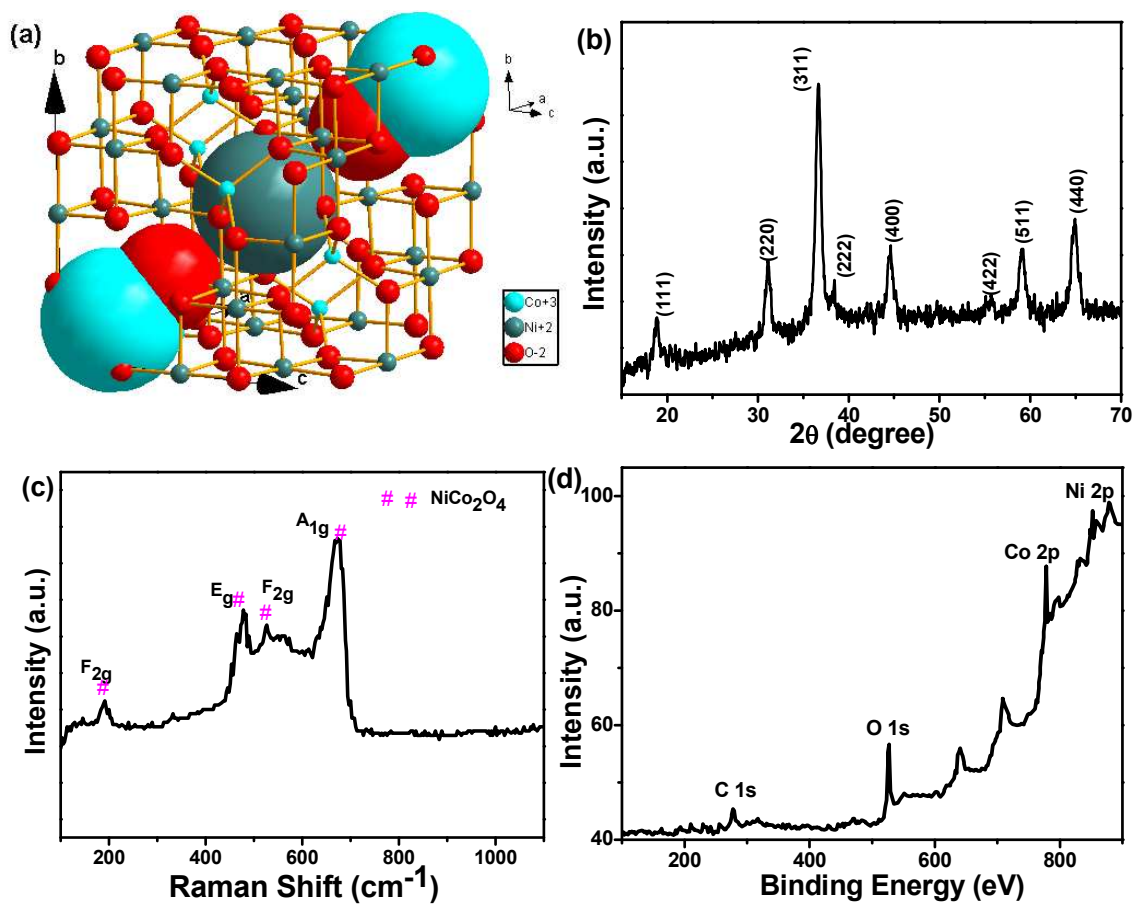


Fig. 4 (a) Crystal structure; (b) XRD pattern; (c) Raman spectra, and (d) XPS survey spectra of NiCo₂O₄.

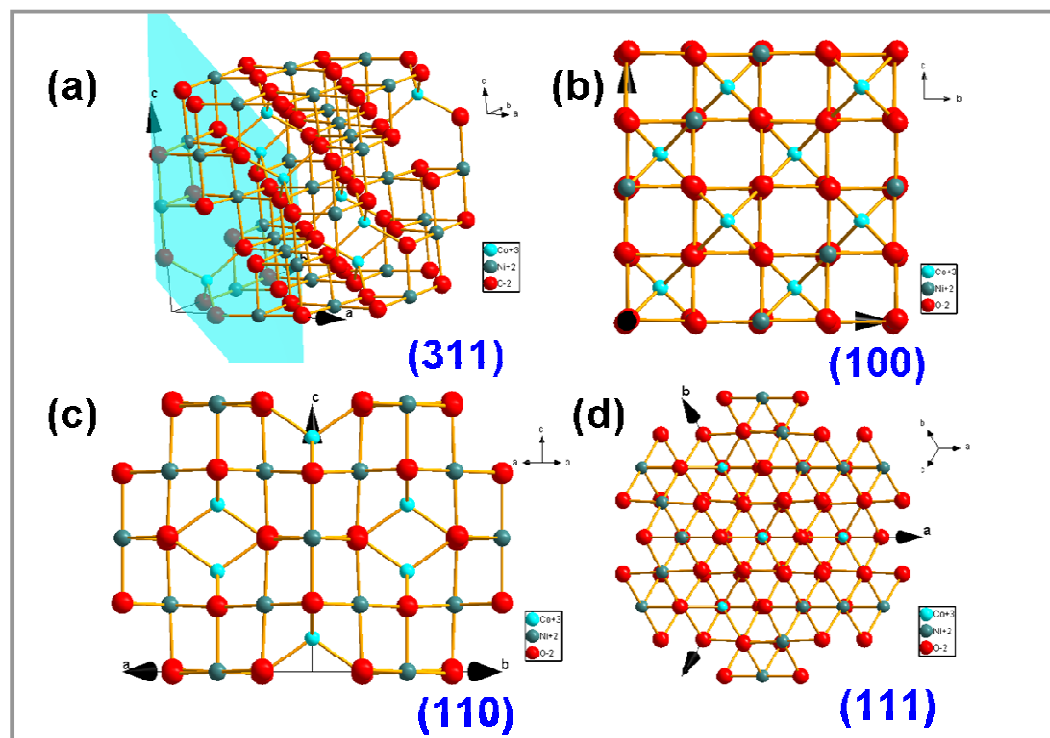


Fig. 5 Schematic diagram of NCONN crystal face. (a) The pale green plane was (311) crystal face; (b-d) were the parallel projection of (100), (110) and (111) crystal face.

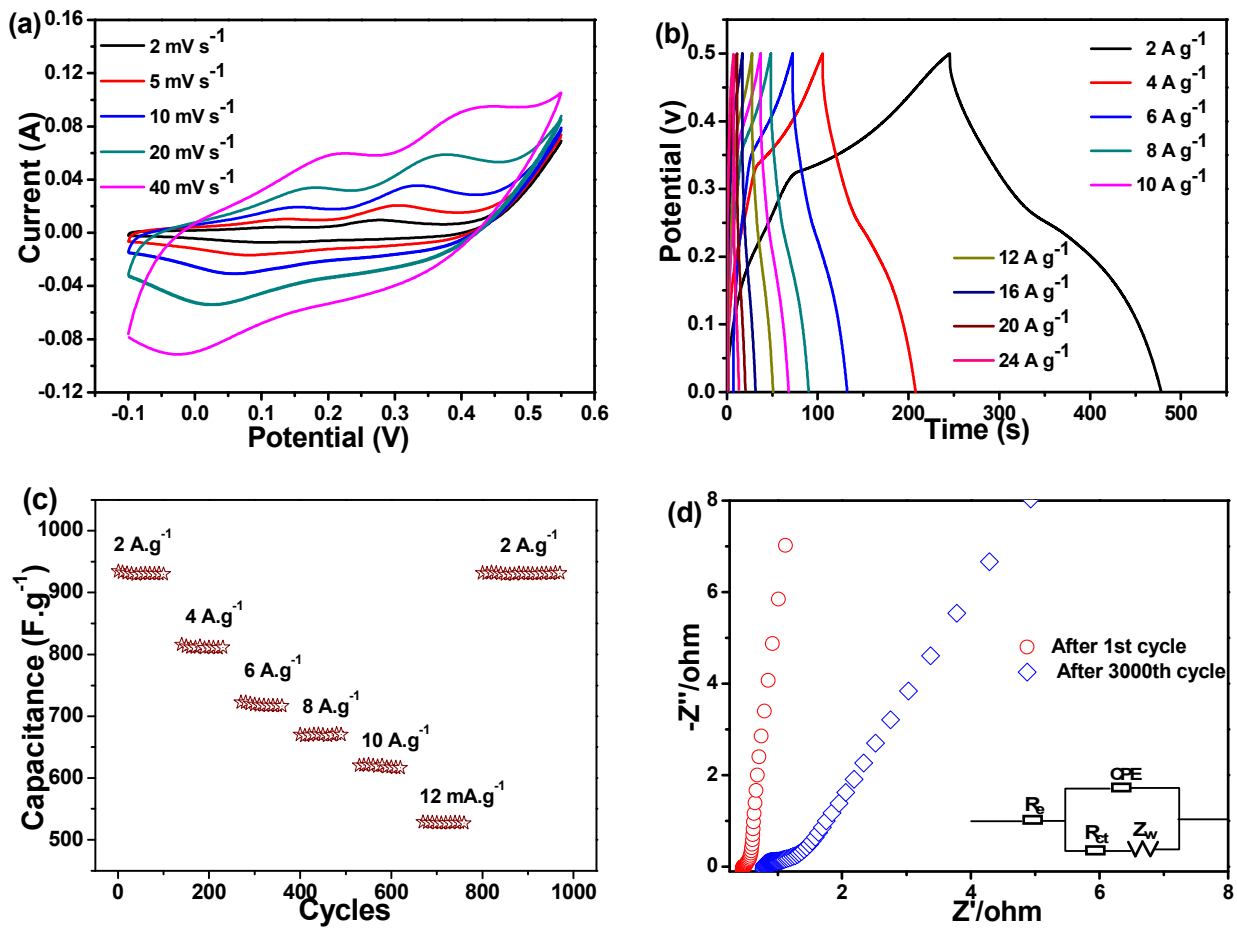


Fig. 6 (a) CV curves of NCONNs at different scan rates; (b) Galvanostatic charge-discharge curves of NCONNs at various current densities; (c) Cycling stability of the NCONNs at progressively various current densities. (d) Electrochemical impedance spectra after 1st and 3000th cycles of NCONNs.

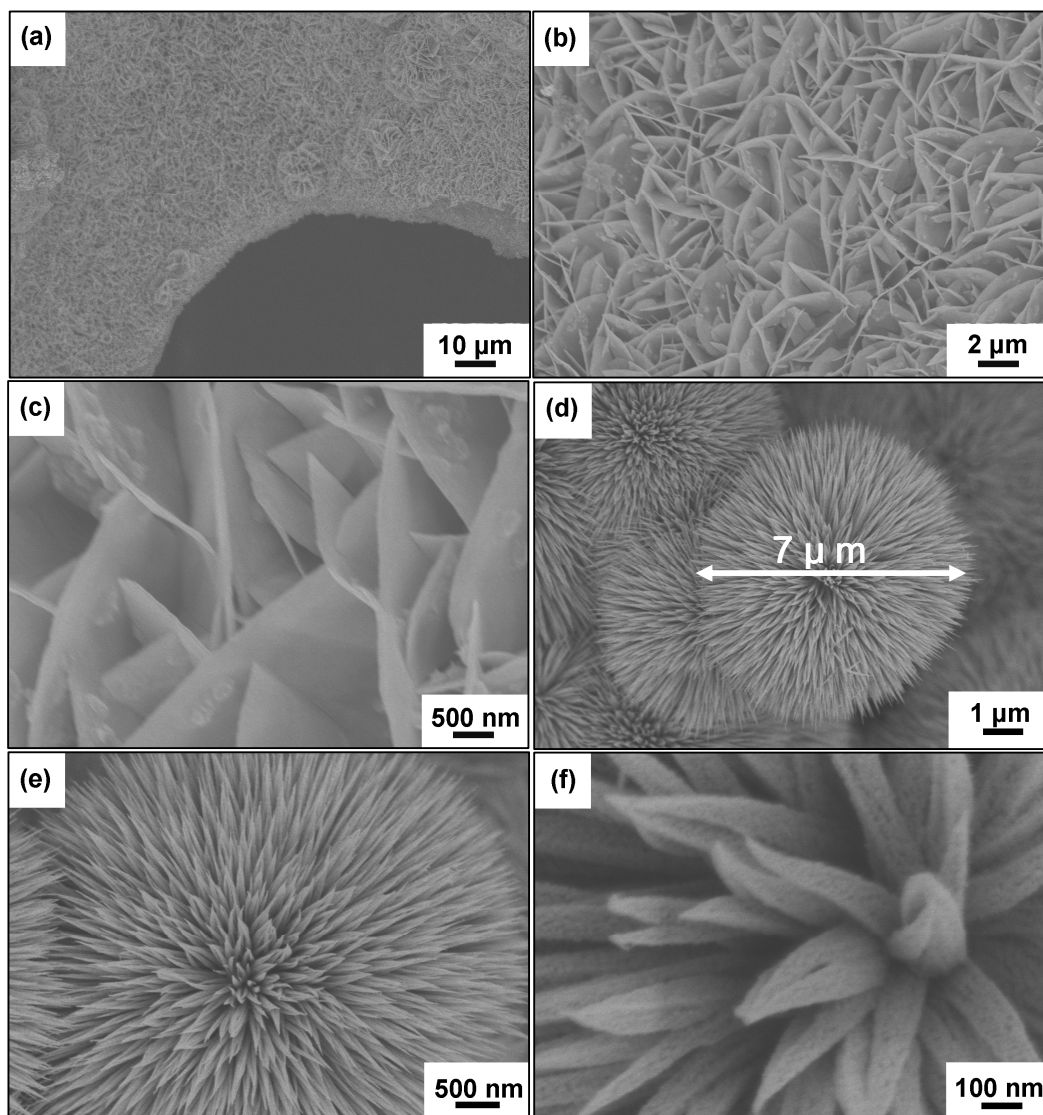


Fig. 7 Temperature-dependent evolution of the NiCo₂O₄ nanostructures at different hydrothermal reaction temperature: (a, b) 120 °C; (c, d) 90 °C; (e, f) 120 °C (prepared in the absence of Ni foam).

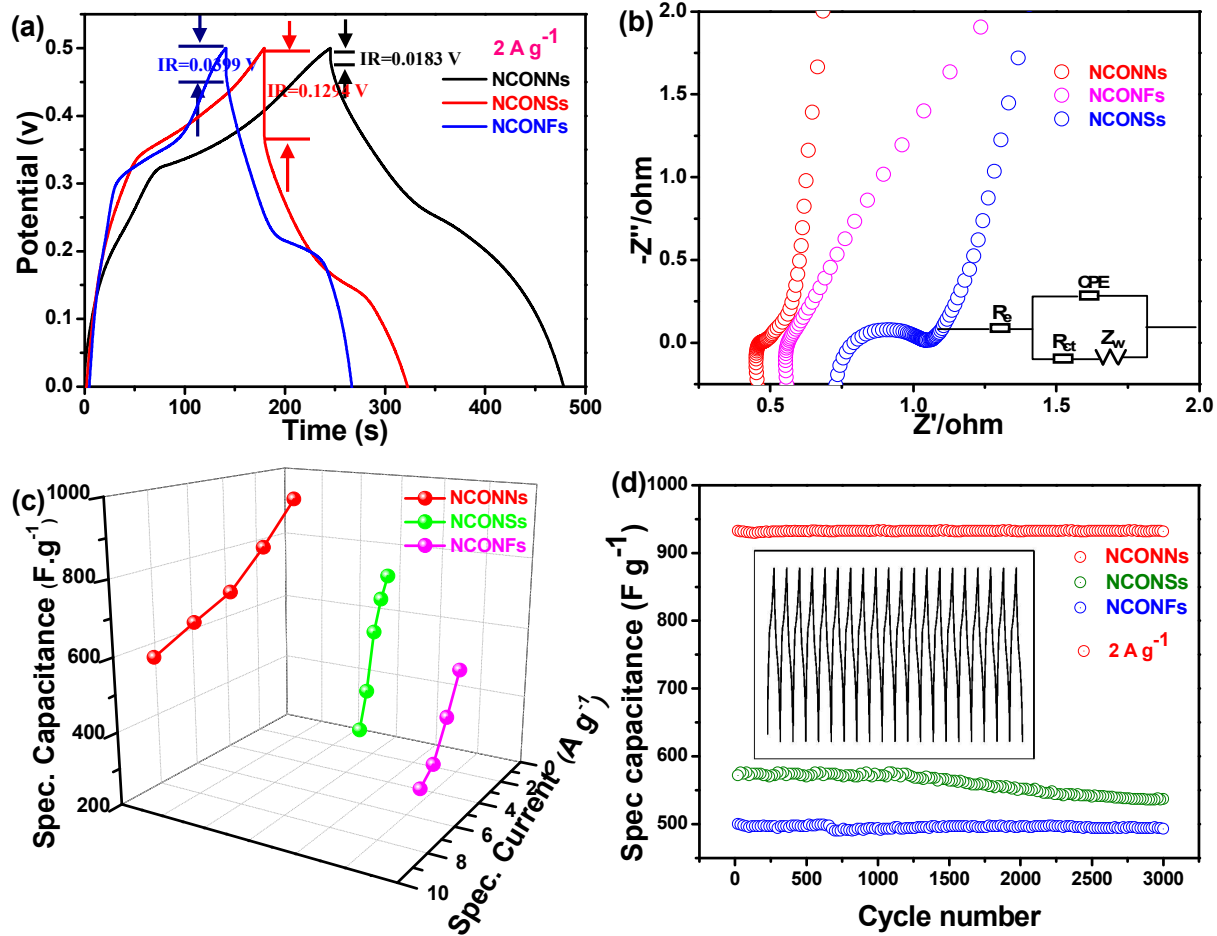


Fig. 8 The electrochemical properties of three kind's materials. (a) Charge-discharge curves, (b) Electrochemical impedance spectra, (c) specific capacitance as a function of current density and (d) cycling performance at current densities of 2 A g^{-1} of NCONNs, NCONFs, NCONSSs.

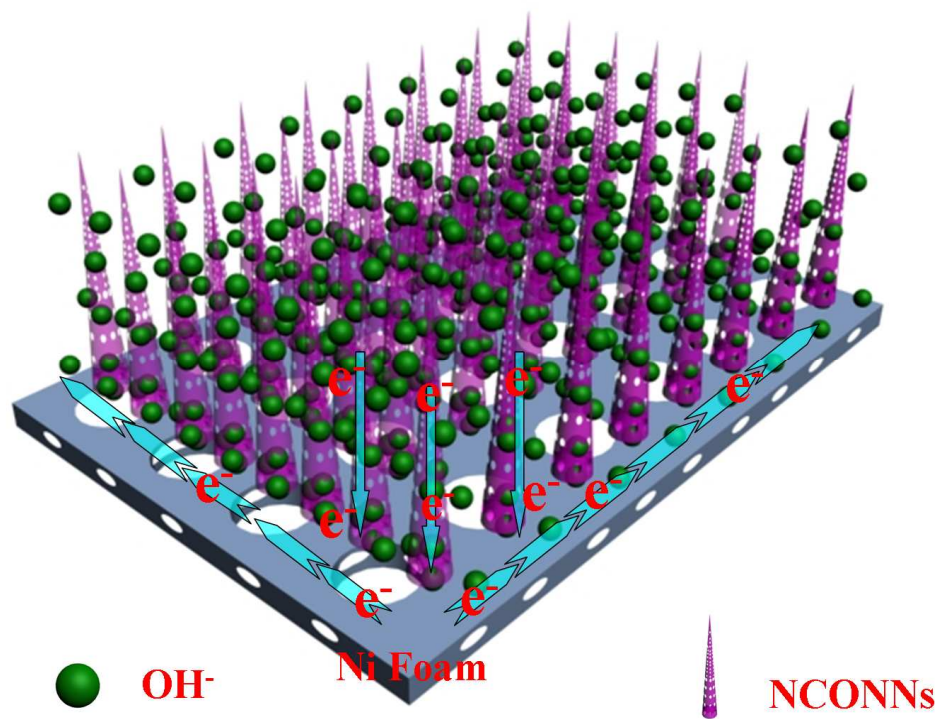
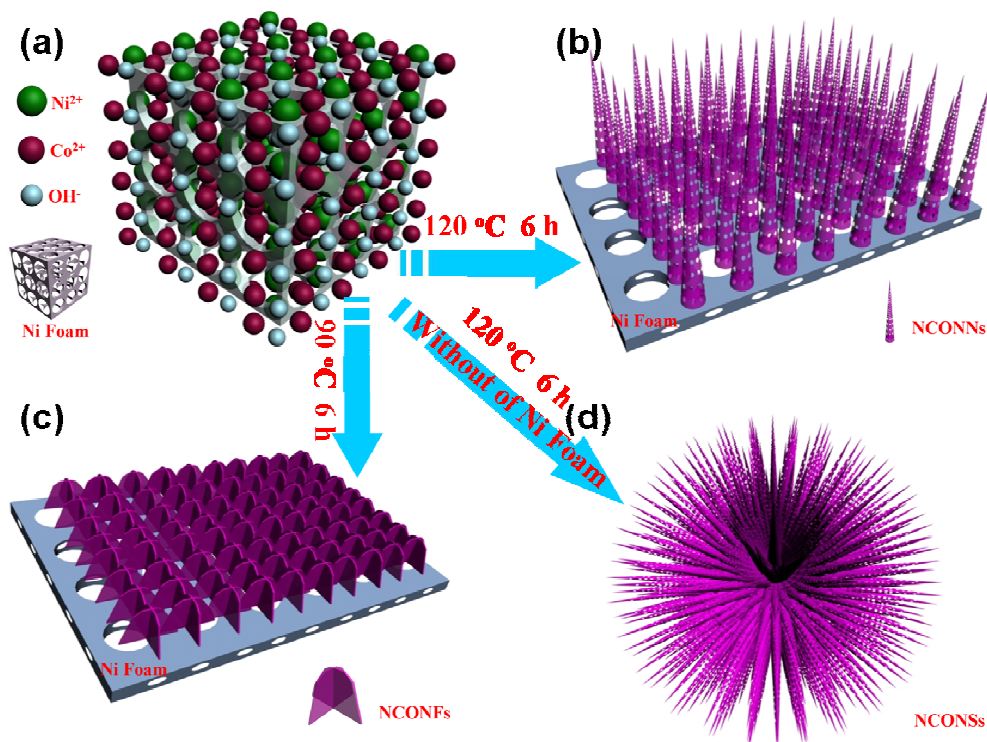


Fig. 9 Schematic diagram showing the kinetic advantages of the hybrid array in electrochemical energy storage.

Graphical Abstract



Three types of NiCo_2O_4 nanostructures, homogeneous NiCo_2O_4 nanoneedle arrays, heterogeneous NiCo_2O_4 nanoflake arrays and NiCo_2O_4 nanoneedle-assembled sisal-like microspheres are synthesized via facile solution methods in combination with thermal treatment. The NiCo_2O_4 nanoneedle arrays are evaluated as supercapacitor electrodes and demonstrate excellent electrochemical performances with high specific capacitance (923 F g^{-1} at 2 A g^{-1}), good rate capability, and superior cycling stability.

NiCo₂O₄ Nanostructures Materials: Morphology Control and Electrochemical Energy Storage

Deyang Zhang^{†a,b,d}, Hailong Yan^{† a,b}, Yang Lu^{†a,b,c}, Kangwen Qiu^{† a,b}, Chunlei Wang^{a,b}, Yihe Zhang^d, Xianming Liu^e, Jingshan Luo^f, Yongsong Luo^{* a,b,f}

^a School of Physics and Electronic Engineering, Xinyang Normal University, Xinyang 464000, P. R. China

^b Key Laboratory of Advanced Micro/Nano Functional Materials, Xinyang Normal University, Xinyang 464000, P. R. China

^c School of Material Science and Engineering, Hebei University of Technology, Tianjin 300130, P. R. China

^d School of Materials Science and Technology, China University of Geosciences, Beijing 100083, P. R. China

^e College of Chemistry and Chemical Engineering, Luoyang Normal University, Luoyang 471022, P. R. China

^f Division of Physics and Applied Physics, School of Physical and Mathematical Sciences, Nanyang Technological University, 637371, Singapore

Abstract

Three types of NiCo₂O₄ nanostructures, homogeneous NiCo₂O₄ nanoneedle arrays, heterogeneous NiCo₂O₄ nanoflake arrays and NiCo₂O₄ nanoneedle-assembled sisal-like microspheres are synthesized via facile solution methods in combination with thermal treatment. The NiCo₂O₄ nanoneedle arrays are evaluated as supercapacitor electrodes and demonstrate excellent electrochemical performances with high specific capacitance (923 F g⁻¹ at 2 A g⁻¹), good rate capability, and superior cycling stability. The superior capacitive performances are mainly due to the unique one dimensional porous nanoneedle architecture, which provides faster ion/electron transfer rate, improved reactivity, and enhanced structural stability. The fabrication method presented here is facile, cost-effective and scalable, which may open a new pathway for real device applications.

* To whom correspondence should be addressed: E-mail: ysluo@xynu.edu.cn

† These authors contribute equally to this work.

1. Introduction

With the increasing demand for clean and renewable energy, more urgent efforts have been

advocated to develop efficient energy storage and conversion devices. Moreover, with the fast development of portable electronic devices with lightweight and flexible designs, the research on flexible storage devices becomes very important. Supercapacitors (SCs) can repeatedly generate electricity from storage materials and convert electric energy into chemical energy reversibly. Due to its outstanding properties, such as high power density, good safety, long cycle life, use of low-cost abundant raw materials and cost-effective synthesis, SCs have been considered as the most successful and prospective technologies for energy storage. 1-7 Previous studies have shown that excellent performance of SCs mainly decided by the type and structure of the electrode materials. However, carbon is still the dominant electrode material for current commercial SCs, which fail to meet the stringent requirements for future large-scale applications.8-11 Accordingly, scientists worldwide are searching for other materials, including transition metal oxides, conducting polymers and hybrid composites to replace or compensate with carbon materials to acquire higher specific capacitance and superior cycle performance. 12-24 It has been well established that nanostructured electrode designs offer unique properties, such as increased active surface areas, short ion transport pathways, better accommodation of the strains, resulting in enhanced power density (or rate capability) and cycling stability of supercapacitors. 25

Recently spinal nickel cobaltite (NiCo_2O_4), replacing one cobalt atom by nickel, has been investigated as a high performance electrode material for SCs owing to its several inherent advantages, including low cost, abundant resources, and good environmental benignity and higher electrochemical activity compared to binary nickel oxide (NiO) and cobalt oxide (Co_3O_4). 26 Thus, NiCo_2O_4 with a broad range of morphologies were fabricated and investigated as the electrode material for SCs, such as nanourchins,27 microspheres, 28 nanosheets, 29 and Nanotubes, 30 the formation of nanocomposites with graphene. 31 For example, Shen et al 27 synthesized urchin-like NiCo_2O_4 nanostructures through a simple hydrothermal method with a high capacitance (1650 F g^{-1} at 1 A g^{-1}) for pseudocapacitor. Srinivasan and co-wokers 30 prepared porous NiCo_2O_4 nanotubes by a single-spinneret electrospinning technique and they exhibit a high specific capacitance (1647 F g^{-1} at 1 A g^{-1}), excellent rate capability (77.3 % capacity retention at 25 A g^{-1}), and outstanding cycling stability (6.4 % loss after 3000 cycles). Traditional electrodes of SCs were typically derived from pasting a homogeneous slurry of nanosized active materials, conductive acetylene black

and polymeric binder onto the current collector, and followed by a solid press treatment. 32 However, it is noteworthy that this kind of electrode design has obvious drawbacks including poor electron transport, the negligence of the advantages of nanoscale size, and low specific capacity caused by the extra weight of additives, 33 which hinder their potential application in high-performance energy storage devices.

Eventhough, a wide variety of nanostructures have been synthesized, tested and acquired excellent performance, it still represents a great challenge to identify the most promising structure that dramatically enhance the supercapacitor performance relative to the high theoretical specific capacitance of NiCo_2O_4 . Previous studies have shown that the charge transfer kinetics to fully utilize the redox reactions in active material can be significantly enhanced by growing either one-dimensional (1D) nanostructures or self-oriented microstructures composed of 1D nanostructures directly over current collectors. 34 In such cases, each nanostructure will have its own electric contact with the substrate. This ensures all nanostructures participate in the electrochemical reaction and avoids the tedious process of mixing active materials with binders. Moreover, internal resistance of the electrode will be reduced as the open space between neighboring microstructures facilitates the diffusion of electrolyte into the inner region of the electrode. 35

Herein, we report a cost-effective and simple strategy to design and fabricate 1D NiCo_2O_4 nanoneedles on Ni foam. In comparison, we also prepared NiCo_2O_4 nanoflakes on Ni foam and NiCo_2O_4 nanoneedle-assembled sisal-like microspheres. NiCo_2O_4 nanoneedle consists of numerous highly crystalline nanoparticles, providing a large number of mesopores for fast ion transport and alleviating the volume change during the charge/discharge process. The flexible $\text{NiCo}_2\text{O}_4/\text{Ni}$ foam can be directly use as a binder-free electrode for supercapacitors, enabling high capacity/capacitance, good cycling stability and excellent rate performance. The fabrication method presented here is facile, cost-effective and scalable, which may open a new pathway for real device applications.36,37

2. Methods

2.1 Synthesis of NiCo_2O_4 nanoneedle arrays (NCONNs) on Ni foam

All the reagents were analytical grade and directly used after purchase without further purification. Prior to deposition, commercial Ni foam ($1.5 \times 4 \text{ cm}$ in rectangular shape) were cleaned by sonication sequentially in acetone, 1 M HCl solution, deionized water, and ethanol

for 15 min each, drying for standby. NCONNs on Ni foam were synthesized via a simple one-pot hydrothermal process. In brief, 4 mmol of $\text{Ni}(\text{NO}_3)_2 \cdot 6\text{H}_2\text{O}$ and 8 mmol of $\text{Co}(\text{NO}_3)_2 \cdot 6\text{H}_2\text{O}$ were dissolved into 75 mL of deionized water, followed by the addition of 15 mmol of urea at room temperature and the mixture was stirred to form a clear dark red solution. Then the mixture was transferred in to a 100 mL Teflon-lined stainless autoclave. Then, the well-cleaned Ni foam was immersed in the mixture, and the autoclave was kept at 120 °C for 6 h. After it was cooled down to room temperature, the product on the Ni foam was taken out and washed with deionized water and ethanol several times and cleaned by ultrasonication to remove the loosely attached products on the surface. After that, the sample was dried at 80 °C for characterization. Similarly, the NiCo_2O_4 nanoflake arrays (NCONFs) on Ni foam were also fabricated at 90 °C and a nanoneedle-assembled sisal-like NiCo_2O_4 microspheres (NCONSs) were fabricated at 120 °C without the addition of Ni foam substrates, respectively. Finally, the as-prepared samples were annealed at 400 °C in air for 2 h.

2.2 Characterization

The crystalline structure and phase purity of the products were identified by X-ray diffraction (XRD) using a D8 Advance (Germany, Bruker) automated X-ray diffractometer system with $\text{Cu-K}\alpha$ ($\lambda = 1.5406 \text{ \AA}$) radiation at 40 kV and 40 mA ranging from 10° to 70° at room temperature. Scanning electron microscopy (SEM) images were obtained using a HITACHI S-4800 microscope (Japan). Transmission electron microscopy (TEM) observations were carried out on a JEOL JEM-2010 instrument in bright field and on a HRTEM JEM-2010FEF instrument (operated at 200 kV). Raman spectra were carried out using WITEC CRM200 Raman system equipped with a 532 nm laser source and a 50× objective lens.

2.3 Electrochemical evaluation

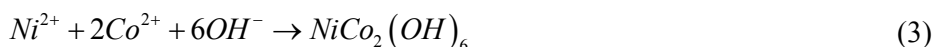
Electrochemical measurements were carried out by electrochemical workstation (CHI 660E, CH Instruments Inc., Shanghai) using three-electrode configuration in 2 M KOH aqueous solution. The value of specific capacitance (F g^{-1}) and current density (A g^{-1}) was calculated based on the total mass of the active materials. The reference and counter electrodes were standard calomel electrode (SCE) and platinum foil, respectively. NCONNs and NCONFs loaded on Ni foam were used directly as the working electrodes and the NCONSs electrode was prepared by mixing the as-prepared samples, acetylene black, and poly-vinylidene

fluoride (PVDF) binder with a weight ratio of 70: 20: 10, which were pasted onto a nickel foam and the electrode was dried under infrared lamp before the electrochemical test. Cyclic voltammetry (CV) measurements were performed at a scanning rate of 2~40 mV s⁻¹ from -0.1 to 0.55 V at room temperature. Galvanostatic charge-discharge measurements were carried out from 0 to 0.5 V at a current density of 2 to 24 A g⁻¹, under open circuit potential. Electrochemical impedance spectroscopy (EIS) measurements were performed by applying an alternate current (AC) voltage with 5 mV amplitude in a frequency range from 0.01 Hz to 100 kHz. The specific capacitances were calculated according to equation $C = (I\Delta t) / (\Delta V \times m)$, where I is the constant discharge current, Δt is the discharge time, ΔV is the voltage drop upon discharging (excluding the IR drop), m is the total mass of the active substance of the electrode material.

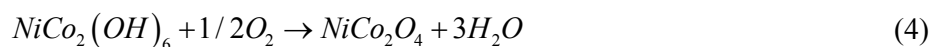
3. Results and discussion

3.1 Morphology and Structural Analysis

The fabrication processes and the resulting novel electrode architectures developed in this work are schematically illustrated in Fig. 1. Ni foam substrates were made by metallic nickel with high flexibility and high conductivity, making them as the unique supporting backbones for controlled growth of NiCo₂O₄ nonmaterial for electrochemical energy storage. NiCo₂O₄ precursor can be easily grown on the highly flexible Ni foam under hydrothermal condition, as described by the following three equations: 8



An annealing treatment at 400 °C with a ramping rate of 2 °C min⁻¹ is utilized to convert the precursor into spinel NiCo₂O₄ supported on the Ni foam, as described by the simple oxidation reaction as follows:



It can be seen that the whole process involves two steps: First, the formation process of NiCo₂(OH)₆ in solution, t a proper pH level realized by controlling the mass of urea and urea

hydrolysis to produce OH^- under the condition of high temperatures. Ni^{2+} and Co^{2+} combined with the OH^- in the solution and through hydrothermal reaction to form NiCo_2O_4 precursors. Second, the obtained precursors were subsequent annealed in air atmosphere. Under various reaction conditions, three kinds of nanostructures were synthesized, 1D nanoneedle arrays (NCONNs) at 120 °C for 6h, 2D nanoflake arrays (NCONFs) at 90 °C for 6h and 3D nanoneedle-assembled sisal-like microspheres (NCONSs) at 120 °C for 6h without of Ni foam (Fig. 1b-d).

The optical images of the NCONNs at different stage are provided in Fig. S1a. Typically, the $\text{NiCo}_2(\text{OH})_6$ precursors were grown directly on substrate and further annealing enabled the formation of micropores. At the same time, the color of the Ni foam substrate changed from silver to amaranth, and black in turns. Fig. S1b and c shows the digital photograph of NCONNs/Ni electrode that can be folded and flexed, demonstrating the good flexibility, which is necessary for flexible device applications.

The morphology of the different products was examined with scanning electron microscopy (SEM). Fig. 2a shows a SEM image of the well-cleaned Ni foam, we can see that the Ni foam has a porous three-dimensional network structure and smooth surface. After the nanoneedle growth, the surface of the whole Ni foam becomes rough as shown in Fig. 2b. After conversion into spinel NiCo_2O_4 , the NCONNs/Ni foam composite still keeps the ordered porous three-dimensional network structure of the Ni foam substrate. Fig. 2c and d demonstrate the higher magnification SEM images of NCONNs at two different magnifications, indicating the large amount loading of the target materials and the homogeneous coverage.. The enlarged view provides the evidence that both the nanoneedle morphology and the array feature of the active materials are perfectly retained after the annealing process. As the samples were ultrasonicated for several minutes before the SEM examination, the uniform coverage of NCONNs on Ni foam confirms that the good adhesion of them on Ni foam. The as-synthesized NCONNs are homogeneously aligned and separated apart adequately. It is expect that this unique structure might have a high surface area and high morphology stability, and this feature could provide high specific capacitance due to the easy access of the active materials in the redox process to their interface, which are highly desirable for high-performance energy storage devices. Typical NCONNs have uniform diameter of about 50 nm and length up to several micrometers.

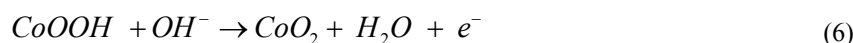
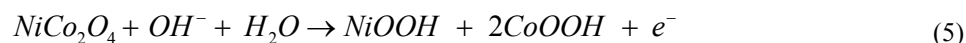
More detailed information about the morphological and structural features of the as-synthesized NCONNs were studied by TEM, HRTEM and selected-area electron diffraction (SAED). From the dispersed nanoneedles as shown in Fig. 3a, it can be seen that

the NCONNs are consisted of porous structures, which results from the release of gas during the decomposition of NCONAs precursor. The porous structures enable facile transport of the electrolyte to the surfaces of NiCo_2O_4 , resulting in rapid charge transfer reactions due to the shortened ions diffusion paths. HRTEM images taken from a single nanocrystal within a nanoneedle are depicted in the inset of Fig. 3a, confirming the polycrystalline nature of the nanoneedles. The clearly resolved lattice fringes were calculated to be about 0.47 nm, 0.28 nm and 0.24 nm, corresponding to the (111), (220) and (311) planes of spinel structured NiCo_2O_4 , respectively. The SAED pattern depicted in Fig. 3b further confirms the polycrystalline nature of the as-obtained NCONNs.

Fig. 4 shows the crystallographic structure, crystallographic phase and the chemical compositions and metal oxidation states of the NCONNs. As depicted in Fig. 4a, the Ni species occupy the octahedral sites and the Co is distributed over both octahedral and tetrahedral sites. Due to the presence of mixed valences of the same cation in such spinel cobaltite, the NiCo_2O_4 possesses at least two orders of magnitude higher electrical conductivity than that of monometallic nickel and cobalt oxides only by electron transfer taking place with relatively low activation energy between cations.³⁸ The crystallographic phase of the as-fabricated NCONNs sample was studied by the XRD technique, and the typical wide-angle diffraction pattern is shown in Fig. 4b. In order to reduce the strong impact of the substrate on the XRD results, the NCONNs were scratched from Ni foam for XRD analysis. Seven well-defined diffraction peaks, including not only the peak positions but also their relative intensities, can be indexed as the cubic spinel NiCo_2O_4 crystalline structure. As the (311) peak has the highest intensity in the XRD patterns, it could infer that NCONNs were grown along the (311) crystal face and the pale green plane in the crystallographic structure is (311) crystal face as shown in Fig. 5a. Fig. 5b-d show the parallel projection of (100), (110) and (111) crystal faces. In order to further understand the composition and structure of these NCONNs samples, Raman analysis was performed and the typical Raman spectra of the products are shown in Fig. 4c. Four peaks of the NCONNs at 187, 477, 523, and 671 cm^{-1} correspond to the F_{2g} , E_g , F_{2g} , and A_{1g} models of NiCo_2O_4 , respectively. These results are consistent with those documented in previous reports.³⁹⁻⁴⁰ The chemical compositions and metal oxidation states of the NCONNs are analyzed by X-ray photoelectron spectroscopy (XPS). A full-survey-scan spectrum in Fig. 4d indicates the presence of Ni, Co, and O, as well as C from the reference and the absence of other impurities.^{28,41}

3.2 Electrochemical properties

The electrochemical storage application of as-prepared NCONNs was evaluated by testing them as binder-free electrodes for supercapacitors. The pseudocapacitive properties of the NCONNs are investigated by cyclic voltammetry (CV) and galvanostatic charge-discharge measurements in three electrode configurations with 2 M KOH aqueous solution as the electrolyte. Fig. 6a shows the typical cyclic voltammetry (CV) curves of the NCONNs electrode with various sweep rates ranging from 2 to 40 mV s⁻¹. The shape of the CV curves clearly confirms the pseudocapacitive behavior, which is distinct from electric double-layer capacitance characterized by nearly rectangular CV curves. Specifically, the redox peaks can be observed within the potential range from -0.1 to 0.55 V (vs. SCE) for all sweep rates, which is mainly related to the faradaic redox reactions related to M–O/M–O–OH (M=Co and Ni ions) in the alkaline electrolyte, as shown in the following equations: 42-44



The peaks are located at around 0.05 and 0.15 V (vs. SCE) when the scan rate is 2 mV s⁻¹. With the 20-fold increase in the sweep rate from 2 to 40 mV s⁻¹, the position of the cathodic peak shifts from 0.05 to -0.15 V (vs. SCE). This indicates the low resistance of the electrode because of the conductive Ni foam substrate.⁴⁵ Furthermore, the peak current increases when increase the scan rate, but the shape of these CV curves does not significantly change as the scan rate increases from 2 to 40 mV s⁻¹, revealing that this electrode architectures enable fast redox reactions for electrochemical energy storage.

Galvanostatic charge-discharge measurements were conducted at various current densities ranging from 2 to 24 A g⁻¹ to further evaluate the pseudocapacitive properties of the as-synthesized self-supported electrode of NCONNs, and the results are shown in Fig. 6b. Specific and areal capacitances were calculated using equation (7).

$$C_{sp} = I \times \Delta t / (m \times \Delta V) \quad (7)$$

where I (A) represents the constant discharge current, m (mg), ΔV (V) and Δt (s) designate the mass of active materials, potential drop during discharge (excluding the IR drop) and total discharge time, respectively. The calculated specific capacitance as a function of the discharge current density is plotted in Fig. S2. On the basis of the above results, the discharge specific capacitance of the NCONNs at 2, 4, 6, 8, 10, 12, 16, 20 and 24 A g⁻¹ are 932, 816,

720, 672, 620, 528, 448, 360 and 288 F g⁻¹, respectively. About 31 % of specific capacity was retained when the current density increased from 2 to 24 A g⁻¹. And NCONNs have similarly behavior on the charge specific capacitance.

The cycle stability of SCs is a crucial parameter for their practical application. In order to understand the synergistic effect in this electrode design, the cycling performance of the NCONNs at progressively increased current density was recorded in Fig. 6c. During the first 100 cycles with a charge discharge density of 2 A g⁻¹, the NCONNs show stable cycle performance and specific capacity as high as 934.6 F g⁻¹. In the following cycles, the charge/discharge rate changes successively. While, the NCONNs materials always demonstrate stable capacitance. With the current rate changing back to 2 A g⁻¹ for the rest of cycles, a capacitance of ~931 F g⁻¹ can be recovered without noticeable decrease, demonstrating excellent rate performance and cycle stability of the electrodes. The loss of specific capacitance may result from ineffective contacts between part of the unstable NCONNs and the substrate, followed by deterioration of the electron transfer and ion diffusion.

To further show the merits of the NCONNs and Ni foam composite material as the electrode material, electrochemical impedance spectra (EIS) were conducted to reveal the electronic conductivity during the redox process. Impedance spectra of the NCONNs electrode material were measured at open circuit potential with an AC perturbation of 5 mV at the frequency range from 0.01 Hz to 100 KHz. Nyquist plots in Fig. 6d are composed of an arc in the high frequency region and a nearly straight line in the low frequency region. Herein, the high-frequency intercept with the X-axis represented the equivalent series resistance (R_s), associated with the sum of the electrolyte solution resistance, the intrinsic resistance of the active material and the contact resistance at the electrode-electrolyte interface. The charge transfer resistance of the electrode (R_{ct}) was calculated from the diameter of the semicircle in the high frequency region, while the straight line at lower frequencies presented the diffusion behavior of ions in the electrode pores. The steeper shape of the sloped line represented an ideal capacitive behavior with the faster diffusion of ions in electrolyte. 40 The measured impedance spectra were analyzed using the complex nonlinear least-squares fitting method on the basis of the equivalent circuit, which is given in the inset of Fig. 6d, Fig. 6d shows the charge transfer resistances (R_{ct}) of the NCONNs electrode after 1st and 3000th cycle, respectively. The R_{ct} value increases only slightly from the 1st to 3000th cycle owing to good contact between the current-collector and nanoneedle arrays. These analyses revealed that the good electrical conductivity and ion diffusion behavior of the NCONNs resulted in the high

performance for SCs.

As a comparison, NCONFs and NCONSs were also been prepared under different reaction conditions. Fig.7a and c show the SEM images of NCONFs at different magnifications, indicating the large area coverage of the target materials and the homogeneous distribution. And the SEM images of the NiCo₂O₄ nanoneedle-assembled sisal-like microspheres (NCONSs) are shown in Fig. 7d and f. To evaluate the capacitive performances of the as-prepared products, the as prepared samples were tested as the anode materials for SCs. Fig. S3 a and c show the CV curves of the NCONSs and NCONFs, and Fig. S3b and d show the galvanostatic charge-discharge curves of them, respectively.

Fig. 8a displays the typical charge-discharge curves of the three electrodes at a current density of 2 A g⁻¹. Evidently, the NCONNs possess much longer discharge time and thus higher capacitance than the NCONFs and NCONSs. Note that these curves have approximately symmetrical shape, which suggest the good electrochemical capacitive characteristic and the superior reversibility of the redox reactions of these electrodes. It can be seen from Fig. 8a that all the discharge curves consist of two sections: a rapid potential drop due to the internal resistance and a sluggish potential decay stemming from the Faradic redox reaction. The nonlinear feature of such charge-discharge curves further verifies the pseudocapacitive behavior of these electrodes. Notably, a smaller IR drop for the NCONNs nanostructures is observed at the beginning of the discharge curve, suggesting a low internal resistance of this morphology.

The Nyquist plots of NCONNs, NCONFs and NCONSs are compared, as shown in Fig. 8(b). A straight oblique line in the low-frequency range can be observed for all the three electrodes. However, in the high-frequency range, the NCONNs nanostructures based electrode has smaller depressed semicircle compared to NCONSs, which corresponds to the charge transfer resistance resulting from the electron diffusion. This is due to the direct growth of NCONNs on a conductive substrate, which could ensure good mechanical adhesion, and more importantly, good electrical connection with the conductive substrate. And the decreased ion diffusion and charge-transfer resistances lead to the improved specific capacitance. Besides this, the real axis intercept of the NCONNs nanostructures is smaller than that of the NCONSs, indicating a much smaller bulk resistance of the NCONSs nanostructures, and it is in agreement with the small IR drop shown in Fig. 8a.

The capacitance of the NCONNs electrodes at various current densities is calculated and depicted in Fig. 8c, and the results were compared with the NCONSs and NCONFs electrodes. Clearly, the NCONNs electrode exhibits higher specific capacitance values than

NCONSs and NCONFs at the same current density. A good cycling stability is crucial for real SCs operation. Thus, following the above tests, the long-term cycling performances of the three different electrodes are recorded as shown in Fig. 8d at a current density of 2 A g^{-1} . A significant specific capacitance loss can be seen for NCONSs electrode, only 93.8 % of the initial capacitance be maintained after 3000 cycles. While for NCONNs electrode, the specific capacitance is perfectly retained with negligible decay, demonstrating its superior cyclic stability performance. The good long-term electrochemical stability of the NCONNs electrode can further be proved from the very stable charge-discharge curves of the last 20 cycles (insert of Fig. 8d). The results showed that the charge curves are still very symmetric to their corresponding discharge counterparts, indicating no significant structural change of the NCONNs electrode during the charge/discharge processes.

Based on abundant electrochemical analysis, the flexible NCONNs and Ni foam composite electrode was proved to exhibit excellent performance for SCs. The greatly enhanced specific capacitance and long-term cycling stability of NCONNs electrode can be attributed to its unique morphology and architecture. As the NCONNs are composed of nanocrystallites and possess mesopores, the transportation of electrolytes through their nanochannels is possibly more feasible for efficient redox reactions during Faradaic charge storage process. And the electronic conductivity of NCONNs electrode is significantly improved by directly connected to the growth substrate, which ensures every nanoneedle participates in the ultrafast electrochemical reaction as shown in Fig. 9. The above results evidently suggest that it is appealing to use configuration of the NCONNs as self-supported electrodes for advanced high performance supercapacitors.

Conclusions

In summary, mesoporous NCONNs were successfully grown on Ni foam substrates with robust adhesion through a general hydrothermal method combined with a simple post-annealing treatment, and they directly served as a binder-free electrode for high performance energy storage devices. The electrode design concept presented here allows each NCONN to have its own electrical contact with the Ni foam substrate and provide facile ion diffusion path by the mesoporous structures in the nanoneedle and the large open space between the neighbor nanodeedle, which ensures every nanoneedle participates in the ultrafast electrochemical reaction. Thus, high specific capacitance of 932 F g^{-1} at 2 A g^{-1} and remarkable cycling stability (negligible specific capacitance decay after 3000 cycles at 2 A

g^{-1}) were achieved by using the as synthesized material as electrochemical capacitor electrodes. As a comparison, we also synthesized NCONFs and NCONSs under difference reaction conditions, and they possess worse performance than NCONNs. More importantly, the electrode design concept here can be easily generalized to grow other mesoporous metal oxides nanostructure on substrates for the fabrication of high-performance energy storage devices.

Acknowledgments

This work was financially supported by the National Natural Science Foundation of China (Nos. U1204501, U1304108 and 11272274), the Science and Technology Key Projects of Education Department Henan Province (No. 13A430758), the Young Backbone Teacher of Xinyang Normal University (Nos. 2013GGJS-18). The authors are indebted to Dr D. L. Xu, Y. X. Liu, for their technical assistances and kind help.

Notes and references

- 1 J. Xu, S. L. Gai, F. He, N. Niu, P. Gao, Y. J. Chen and P. P. Yang, Dalton Trans., 2014, **43**, 11667-11675.
- 2 Y. Wang, C. X. Guo, J. Liu, T. Chen, H. Yanga and C. M. Li, Dalton Trans., 2011, **40**, 6388-6391.
- 3 J. L. Shi, W. C. Du, Y. X. Yin, Y. G. Guo and L. J. Wan, J. Mater. Chem. A, 2014, **2**, 10830-10834.
- 4 P. Poizot and F. Dolhem, Energy Environ. Sci., 2011, **4**, 2003-2019.
- 5 L. Wei, C. Li, H. Chu and Y. Li, Dalton Trans., 2011, **40**, 2332-2337.
- 6 B. Duong, Z. N. Yu, P. Gangopadhyay, S. Seraphin, N. Peyghambarian and J. Thomas, Advanced Materials Interfaces, DOI: 10.1002/admi.201300014.
- 7 H. Pang, J. W. Deng, J. M. Du, S. J. Li, J. Li, Y. H. Ma, J. S. Zhang and J. Chen, Dalton Trans., 2012, **41**, 10175-10181.
- 8 L. F. Shen, Q. Che, H. S. Li and X. G. Zhang, Adv. Funct. Mater., 2013, DOI: 10.1002/adfm. 201303138.
- 9 K. Jost, C. R. Perez, J. K. McDonough, V. Presser, M. Heon, G. Dion and Y. Gogotsi, Energy Environ. Sci., 2011, **4**, 5060-5067.
- 10 M. V. Reddy, G. V. Subba Rao, B. V. R. Chowdari, Chem. Rev., 2013, **113**, 5364-5457.
- 11 P. Simon, Y. Gogotsi, Nat. Mater., 2008, **7**, 845-854.
- 12 Y. S. Luo, J. S. Luo, J. Jiang, W. W. Zhou, H. P. Yang, X. Y. Qi, H. Zhang, H.J. Fan, Y. W. Y Denis, C. M. Li and T. Yu, Energy Environ Sci., 2012, **5**, 6559-6566.

- 13 J. P. Liu, J. Jiang, C. W. Cheng, H. X. Li, J. X. Zhang, H. Gong, H. J. Fan, *Adv Mater.*, 2011, **23**, 2076-2081.
- 14 Y. S. Luo, J. Jiang, W. W. Zhou, H. P. Yang, J. S. Luo, X. Y. Qi, H. Zhang, D. Y. W. Yu, C. M. Li and T. Yu, *J Mater Chem.*, 2012, **22**, 8634-8640.
- 15 L. F. Hu, L.M. Wu, M.Y. Liao, X. H. Hu, X. S. Fang, L. Hu, L. Wu and M. Liao, *Adv Funct Mater.*, 2012, **22** 998-1004.
- 16 Y. S. Luo, J. S. Luo, W. W. Zhou, X. Y. Qi, H. Zhang, Y. W. Y. Denis, C. M. Li, H. J. Fan and T. Yu, *J. Mater. Chem. A.*, 2013, **1**, 273-281.
- 17 C. Zhou, Y. W. Zhang, Y. Y. Li, J. P. Liu, *Nano Letters.*, 2013, **13**, 2078-2085.
- 18 Y. S. Luo, D. Z. Kong, J. S. Luo, S. Chen, D. Y. Zhang, K. W. Qiu, X. Y. Qi, H. Zhang, C. M. Li and T. Yu, *RSC Adv.* 2013, **3**, 14413-14422.
- 19 J. Jiang, Y. Y. Li, J. P. Liu, X. T. Huang, C. Z. Yuan and X. W. Lou, *Adv Mater.*, 2012, **24**, 5166-5180.
- 20 D. Z. Kong, J. S. Luo, Y. L. Wang, W. N. Ren, T. Yu, Y. S. Luo, Y. P. Yang and C. W. Cheng, *Adv. Func. Mater.*, 2014, DOI:10.1002/adfm.201304206.
- 21 J. Jiang, Y. Y. Li, J. P. Liu, X. T. Huang, *Nanoscale.*, 2011, **3**, 45-58.
- 22 Y. S. Luo, D. Z. Kong, Y. L. Jia, J. S. Luo, Y. Lu, D. Y. Zhang, K. W. Qiu, C. M. Li and T. Yu, *RSC Adv.*, 2013, **3**, 5851-5859.
- 23 J. S. Luo, X. H. Xia, Y. S. Luo, C. Guan, J. L. Liu, X. Y. Qi, C. F. Ng, T. Yu, H. Zhang and H. J. Fan, *Adv. Energy Mater.*, 2013 **3**, 737-743.
- 24 J. S. Luo, J. L. Liu, Z. Y. Zeng, C. F. Ng, L. J. Ma, H. Zhang, J. Y. Lin, Z. X. Shen and H. J. Fan *Nano Lett.*, 2013 **13**, 6136-6143.
- 25 D. Y. Zhang, H. L. Yan, Y. Lu, K. W. Qiu, C. L. Wang, C. C. Tang, Y. H. Zhang, C. W. Cheng and Y. S. Luo, *Nanoscale Res Lett.*, 2013, **9**, 139-147.
- 26 T. Y. Wei, C. H. Chen, H. C. Chien, S. Y. Lu and C. C. Hu, *Adv. Mater.*, 2010, **22**, 347-351.
- 27 Q. F. Wang, B. Liu, X. F. Wang, S. H. Ran, L. M. Wang, D. Chen and G. Z. Shen, *J. Mater. Chem.*, 2012, **22**, 21647-21653.
- 28 J. F. Li, S. L. Xiong, Y. R. Liu, Z. C. Ju and Y. T. Qian, *ACS Appl. Mater. Interfaces.*, 2013, **5**, 981-988.
- 29 X. H. Lu, X. Huang, S. L. Xie, T. Zhai, C. S. Wang, P. Zhang, M. H. Yu, W. Li, C. L. Liang and Y. X. Tong, *J. Mater. Chem.*, 2012, **22**, 13357-13364.

- 30 L. L. Li, S. J. Peng, Y. L. Cheah, P. F. Teh, J. Wang, G. Wee, Y. W. Ko, C. L. Wong and M. Srinivasan, *Chem. Eur. J.*, 2013, **19**, 5892-5898.
- 31 S. Chen and S. Z. Qiao, *ACS nano*, 2013, **7**, 10190-10196.
- 32 L. W. Ji and X. W. Zhang, *Electrochem. Commun.*, 2009, **11**, 1146-1149.
- 33 C. C. Hu, K. H. Chang, M. C. Lin and Y. T. Wu, *Nano Lett.*, 2006, **6**, 2690-2695.
- 34 X. X. Qing, S. Q. Liu, K. L. Huang, K. Z. Lv, Y. P. Yang, Z. G. Lu, D. Fang, X. X. Liang, *Electrochim. Acta*, 2011, **56**, 4985-4991.
- 35 R. B. Rakhi, W. Chen, D. Cha and H. N. Alshareef, *Nano letters*, 2012, **12**, 2559-2567.
- 36 X. S. Fang, T. Y. Zhai, U. K. Gautam, L. Li, L. M. Wu, Y. Bando, D. Golberg, *Prog Mater Sci.*, 2011, **56**, 175-287.
- 37 X. S. Fang, L. F. Hu, K. F. Huo, B. Gao, L. J. Zhao, M. Y. Liao, P. K. Chu, Y. Bando, D. Golberg, *Adv Funct Mater.*, 2011, **21**, 3907-3915.
- 38 T. Y. Wei, C. H. Chen, H. C. Chien, S. Y. Lu and C. C. Hu, *Adv. Mater.*, 2010, **22**, 347-351.
- 39 Z. A. Hu, Y. L. Xie, Y. X. Wang, L. J. Xie, G. R. Fu, X. Q. Jin and H. Y. Wu, *J. Phys. Chem. C.*, 2009, **113**, 12502-12508.
- 40 J. H. Zhong, A. L. Wang, G. R. Li, J. W. Wang, Y. N. Ou and Y. X. Tong, *J. Mater. Chem.*, 2012, **22**, 5656-5665.
- 41 C. Z. Yuan, J. Y. Li, L. R. Hou, L. Yang, L. F. Shen, X. G. Zhang, *J. Mater. Chem.*, 2012, **22**, 16084-16090.
- 42 X. Wang, X. D. Han, M. F. Lim, N. Singh, C. L. Gan, J. Ma and P. S. Lee, *J. Phys. Chem. C.*, 2012, **116**, 12448-12454.
- 43 V. Gupta, S. Gupta and N. Miura, *J. Power Source*, 2008, **175**, 680-685.
- 44 C. C. Hu and C. Y. Cheng, *J. Electrochem. Solid-State Lett.*, 2002, **5**, A43-A46.
- 45 G. Q. Zhang, H. B. Wu, H. E. Hoster, M. B. C. Park, X. W. Lou, *Energy Environ Sci.*, 2012, **5**, 9453-9456.